Effects of polymer solutions on hydraulic fracture

Yujing Du [1,2,*] Thomas Cochard [2] Ilya Svetlizky [3] Congcong Yuan [2,4] Yiqiao Song [2,5] Lizhi Xiao [6,†] and David Weitz [2,7,‡]

[1]*College of Engineering and Computer Science, The University of Tulsa, Tulsa, Oklahoma 74104, USA*
[2]*John A. Paulson School of Engineering and Applied Sciences, Harvard University, Cambridge, Massachusetts 02138, USA*
[3]*Department of Physics, Technion—Israel Institute of Technology, Haifa 3200003, Israel*
[4]*School of Civil and Environmental Engineering, Nanyang Technological University, Singapore 639798, Singapore*
[5]*Athinoula A. Martinos Center for Biomedical Imaging, Department of Radiology, Massachusetts General Hospital, Charlestown, Massachusetts 02129, USA*
[6]*National Key Laboratory of Petroleum Resources and Engineering, China University of Petroleum (Beijing), Beijing 102249, China*
[7]*Department of Physics, Harvard University, Cambridge, Massachusetts 02138, USA*

(Received 2 November 2025; accepted 7 January 2026; published 26 January 2026; corrected 1 June 2026)

Polymer solutions are widely used in hydraulic fracturing operations to enhance proppant transport, suppress turbulence, and reduce fluid loss. However, how their properties influence the local flow field and fracture dynamics, especially in the rapidly evolving region near the fracture tip, remains poorly understood. This study investigates the coupled fluid flow and fracture behavior near the tip of a propagating hydrofracture driven by polymer solutions using high-speed imaging within a transparent, three-dimensional-printed polymethyl methacrylate model. Solutions of high-molecular-weight polymers induce flow and fracture behavior that closely resemble those of water, while viscous Newtonian fluids produce different behavior. This is attributed to pronounced shear thinning, which significantly lowers the effective viscosity under high shear and hence alters the local flow field and stress distribution near the fracture tip. These findings underscore the importance of fluid rheology in shaping both flow patterns and fracture development during hydraulic fracturing.

DOI: 10.1103/p4bp-b8bz

I. INTRODUCTION

A hydrofracture is a fracture of a solid medium initiated and driven by elevated fluid pressure within the material [1]. Hydrofractures can be induced by both natural and engineered causes. In natural geological environments, locally pressurized fluids trapped in rock formations can induce fractures during seismic events [2]. In engineered environments such as geothermal energy extraction [3,4] and oil and gas recovery [5–8], hydrofractures are deliberately created by high-pressure fluid injections that enhance the recovery of heat or subsurface resources. In all cases, hydrofracturing occurs when the fluid pressure within the material exceeds its tensile strength [1]. In engineering applications, the process is widely known as hydraulic fracturing or fracking [9]. In these cases, the nature of the fracturing fluid plays a critical role in the effectiveness of the operation. Polymer solutions are commonly used as the fracturing fluid as they can form a gel that plugs the pores, reducing fluid loss from the fracture into the surrounding formation [10]. Polymer solutions also suppress turbulence during pipe flow, reducing frictional pressure losses and lowering the energy required for pumping [11]. In addition, polymer solutions can improve the transport and suspension of proppants, which are high-strength particles such as sand or ceramics coinjected with the fluid to keep the fractures open [12]. However, polymer solutions exhibit complex rheological properties, such as shear thinning and viscoelasticity, which differ significantly from those of water and other Newtonian fluids [13–18]. Measurements of the consequences of these rheological properties are difficult to perform in the field; instead, controlled laboratory experiments using transparent, well-characterized model systems are required. Studies using transparent materials such as hydrogels and plastics have enabled the initiation and propagation of a fluid-driven fracture to be directly observed under controlled, reproducible conditions [19–22]. These model systems make it possible to isolate the effects of fluid properties and gain mechanistic insight into the coupled dynamics of flow and fracture. Nevertheless, the flow and fracture behavior of polymer solutions near the tip of a propagating hydrofracture remains poorly understood. This lack of understanding hinders our ability to accurately quantify local stress fields and predict fracture propagation [23,24], which are essential for guiding the design and optimization of polymer solutions for hydraulic fracturing.

In this paper, we use a three-dimensional (3D)-printed poly(methyl methacrylate) (PMMA) cylindrical sample and induce a penny-shaped hydrofracture by injecting polymer solutions at high pressure and visualize the flow and fracture

*Contact author: yujingdu@utulsa.edu
†Contact author: xiaolizhi@cup.edu.cn
‡Contact author: weitz@seas.harvard.edu

Published by the American Physical Society under the terms of the Creative Commons Attribution 4.0 International license. Further distribution of this work must maintain attribution to the author(s) and the published article's title, journal citation, and DOI.

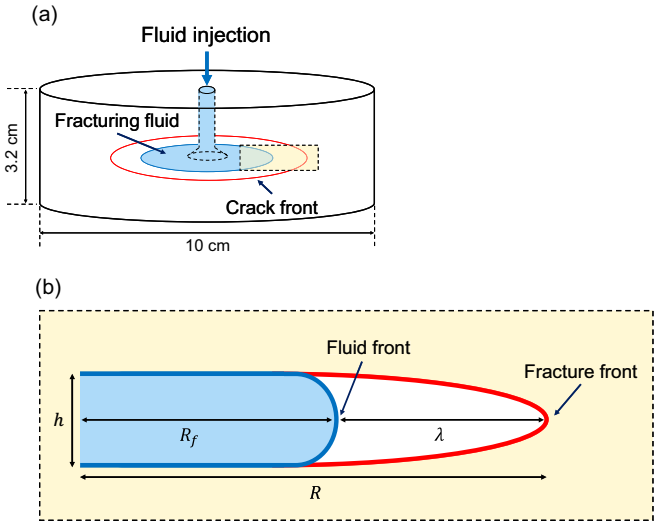

FIG. 1. Schematic of the experimental setup and fracture geometry. (a) A 3D-printed PMMA cylindrical sample is placed horizontally on a transparent acrylic sheet. A penny-shaped hydrofracture is initiated at the notch at the bottom of the inlet hole by injecting fracturing fluids using a high-pressure syringe pump. The fracture propagates approximately along the horizontal plane and is recorded from below using a high-speed camera with a temporal resolution ranging from 10 to 19 μs across different experiments. Fracture initiation is detected by acoustic emission sensors, which trigger the camera for synchronized imaging. The PMMA material has a Young's modulus of approximately 2.9 GPa and a density of 1200 kg/m^3. (b) Schematic side view of the fracture geometry with a viscous hydrofracturing fluid, showing the position of the fracture front (red), fluid front in (blue), fracture radius R, fluid radius R_f, fracture aperture h, and fluid lag λ between the fluid and fracture fronts. The value of λ varies depending on the hydrofracturing fluid used.

dynamics using high-speed imaging. We find that polymer solutions significantly modify the local flow and fracture dynamics compared to Newtonian fluids. We investigate the behavior of solutions of polymers with a wide range of molecular weights. Remarkably, high-molecular-weight polymer solutions exhibit behavior very similar to that of water, a Newtonian fluid, despite their fundamentally different properties and viscosities. This behavior is attributed to pronounced shear thinning at the very high shear rates near the fracture tip. These results reveal a regime of fluid-fracture interaction governed by polymer rheology.

II. DISTINCT FLOW AND FRACTURE BEHAVIOR OF POLYMER SOLUTIONS COMPARED TO NEWTONIAN FLUIDS

To investigate the fracturing behavior with the polymer solutions, we inject fracturing fluids at high pressure into transparent cylindrical samples fabricated from PMMA-based resin to induce penny-shaped fractures and visualize the process. The experimental platform is schematically illustrated in Fig. 1 [19]. The samples are fabricated using stereolithography, a 3D printing technique that cures liquid photopolymer resin layer by layer with ultraviolet laser light. Clear Resin V4, a transparent PMMA-based resin, is used to print samples with a Formlabs Form 3 printer. Once cured, the material exhibits a Young's modulus of approximately 2.9 GPa and a density of 1200 kg/m^3. The cylindrical sample shown in Fig. 1(a) measures 10 cm in diameter and 3.2 cm in height and has a vertical hole 0.4 cm in diameter at the center, with a 1 cm circular notch at the bottom to facilitate controlled fracture initiation. Images of the sample taken under natural light, illustrating its true color and transparency, are provided in Sec. I of the Supplemental Material [25].

In each experiment, the sample is placed horizontally on an acrylic sheet. Fracturing fluid is injected into the sample through the hole at the center using a Teledyne ISCO high-pressure syringe pump at a constant rate of 0.03 ml/min. When the pressure reaches approximately 25 MPa, a penny-shaped fracture is initiated from the notch and propagates horizontally toward the boundary of the sample. At this low injection rate, fluid flow within the propagating fracture is driven by expansion of the pressurized fluid, rather than by continued volumetric injection. All experiments are conducted under ambient laboratory temperature.

The fracture process is recorded from beneath the sample using a Phantom TMX5010 high-speed camera equipped with a Rokinon 35 mm T1.5 VDSLR lens. The imaging system achieves a temporal resolution of 10–19 μs and a spatial resolution of 140–200 μm/pixel, depending on the specific experimental setup. A fluorescent dye is added to the fluid to enable visualization during subsequent image analysis.

To establish a baseline for studying the hydrofracturing process with polymer solutions, we review the behavior of Newtonian fluids with varying viscosities by using different glycerol-water mixtures. For pure water with the lowest viscosity, the fluid front closely follows the fracture front with a minimal distance, as shown in the fracture plane captured 2000 μs after the fracture initiation in Fig. 2(a). The corresponding kymograph in Fig. 3(a), generated by plotting light intensity along a radial direction over time, confirms that both fronts propagate smoothly. For more viscous fluids, such as the 95 wt % glycerol-water mixture with a viscosity of 0.4 Pa s, the fluid front lags significantly behind the fracture front, as illustrated in Fig. 2(b). The lag length, λ, is illustrated schematically in Fig. 1(b). The kymograph in Fig. 3(b) shows that the fracture advances in a discrete steplike, or stick-break manner, while the fluid progresses smoothly. As the fluid viscosity increases from 0.05 to 1 Pa s, λ varies from 0.5 to over 10 mm, as shown in Fig. 4(a), likely because higher viscosity slows fluid flow, allowing the fracture to outpace the fluid. The larger lag also leads to greater break amplitudes, as the same relative increase in effective stress intensity corresponds to a greater fracture propagation distance. These observations agree with the lag predicted from a linear elastic fracture mechanics (LEFM)-based analytical model assuming Poiseuille flow, which integrates fluid pressure along the fracture to compute the effective stress intensity factor and the resulting lag for Newtonian fluids [19]. In this model, fracture propagation is governed by a Griffith-type criterion: The fracture advances only when the effective stress intensity factor exceeds the critical fracture toughness of the PMMA material and arrests when it falls below this threshold. The observed stick-break behavior therefore reflects repeated crossings of this critical

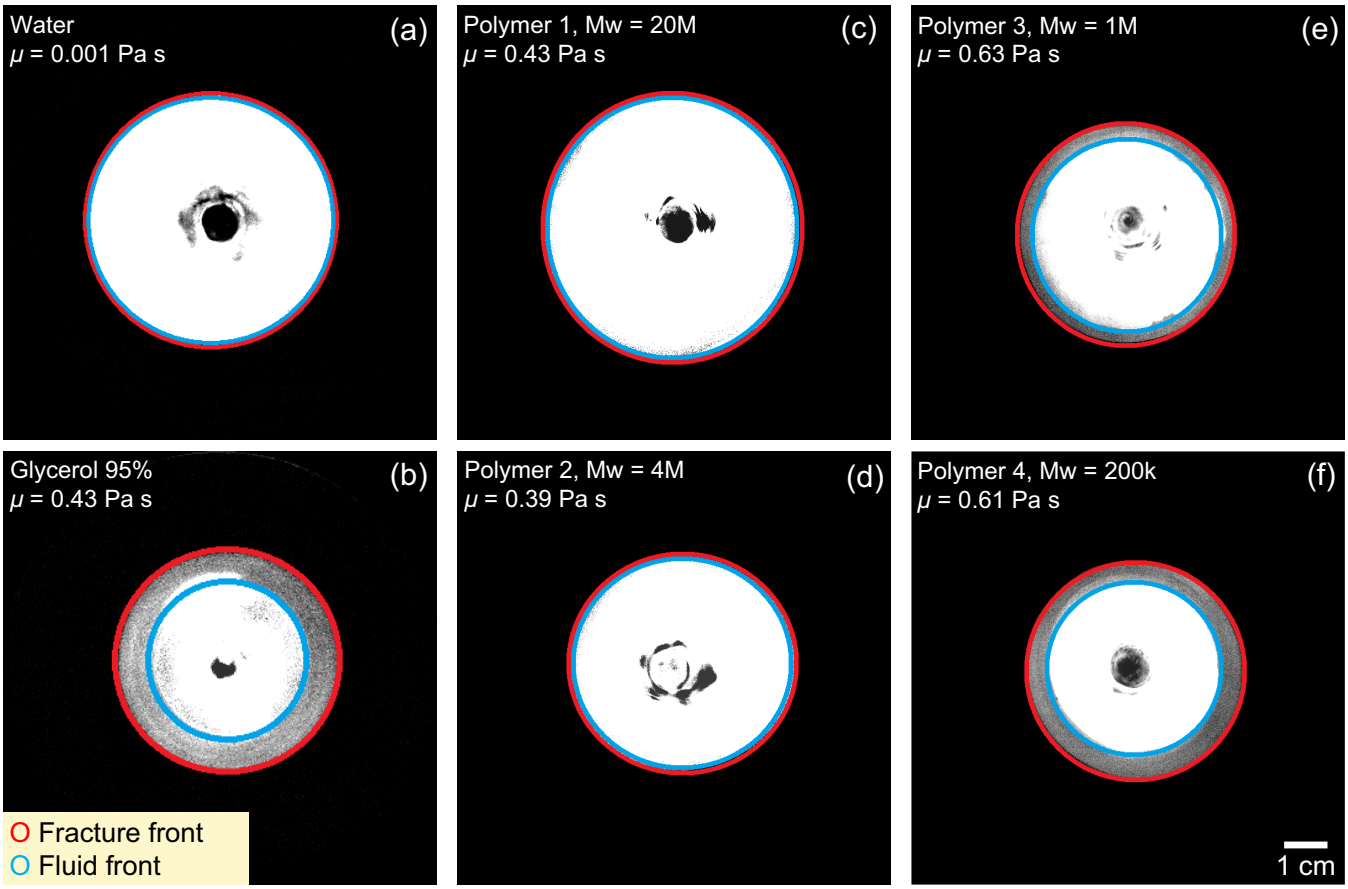

FIG. 2. Images of the fracture plane captured from beneath the sample show the hydrofracture patterns for six different fracturing fluids. The red and blue contours denote the fracture front and the fluid front, respectively. Fluorescent dye is added to all fluids, making them the brightest phase in each image. Under back illumination, the fractured region appears brighter (gray) than the intact material because the opening of an internal fracture gap increases light transmission relative to the intact material. All images are captured 2000 μs after fracture initiation to avoid nucleation and boundary effects. The fracturing fluids in each image are (a) water, where the fluid front and the fracture front are very close; (b) 95 wt % glycerol-water mixture with a viscosity of 0.43 Pa s, where the fluid front lags significantly behind the fracture front; (c) Polymer 1 with a molecular weight of 20M g/mol and a viscosity of 0.43 Pa s, where the fluid front and the fracture front are very close, similar to water; (d) Polymer 2 with a molecular weight of 4M g/mol and a viscosity of 0.39 Pa s, where the fluid front and the fracture front are very close, also similar to water; (e) Polymer 3 with a molecular weight of 1Mg/mol and a viscosity of 0.63 Pa s, where the fluid front lags slightly behind the fracture front; and (f) Polymer 4 with a molecular weight of 200k g/mol and a viscosity of 0.61 Pa s, where the fluid front lags further behind the fracture front but with smaller lag compared to the 95 wt % glycerol-water mixture. The fracturing fluids used in panels (b)–(f), including four polymer solutions and a glycerol-water mixture, are selected to have comparable viscosities at the low shear rate at which they were characterized. The scale bar represents 1 cm, and the sample diameter is 10 cm. The temporal resolution is 10.3 μs in panel (a), 13.4 μs in panel (b), and 19.3 μs in panels (c)–(f). The spatial resolution is 200 μm in panel (a) and 140 μm in panels (b)–(f).

threshold, with elastic energy accumulating during arrest and being released during rapid break events, fully consistent with LEFM predictions and without invoking plastic effects. The experiments are consistent with prior simulations based on LEFM and cohesive-zone modeling, and future work could extend this framework to explore the influence of temperature on fracture mechanics [26,27] and to enable further comparisons with theories and simulations [28–30].

To explore fracture behavior using polymer solutions, we use a hydrolyzed polyacrylamide polymer with a high molecular weight of 20M g/mol. We prepare a polymer solution with a concentration of 0.2 wt %; it has a viscosity of 0.43 Pa s at a low shear rate of $1\,s^{-1}$. This viscosity is comparable to that of the 95 wt % glycerol-water mixture, whose viscosity is 0.4 Pa s. Surprisingly, the fluid front of the polymer solution, outlined in blue, closely follows the fracture front, outlined in red, with only a narrow gap between them, as shown in Fig. 2(c). Moreover, both the fracture and the polymer solution fronts propagate smoothly with a consistently small lag length of approximately 0.5 mm, as seen in the kymograph in Fig. 3(c). This behavior is unexpectedly similar to that with water, which has a much lower viscosity, and is in sharp contrast with the large lag lengths and break amplitudes observed in glycerol-water mixtures with comparable viscosities to the polymer solution.

To test the consistency of this behavior, we use another hydrolyzed polyacrylamide polymer with a lower molecular weight of 4M g/mol. We prepare a solution with a concentration of 0.6 wt %; it has a viscosity of 0.39 Pa s at a low shear rate of $1\,s^{-1}$, comparable to that of the higher

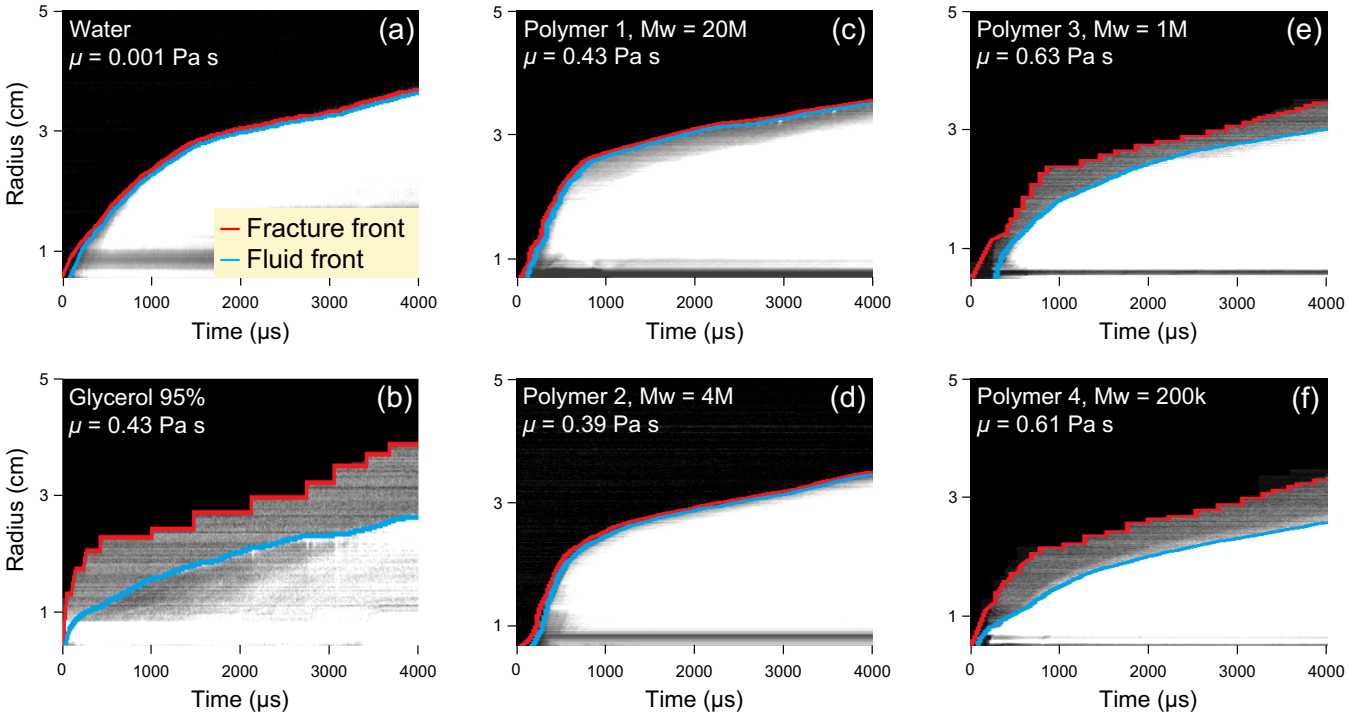

FIG. 3. Kymographs show the spatiotemporal evolution of fluid and fracture fronts in the penny-shaped hydrofracture for six different fracturing fluids. The red and blue contours denote the fracture front and the fluid front, respectively. Fluorescent dye is added to the fluids to enhance optical contrast; in panel (b), imperfect dye mixing leads to locally reduced intensity, but the fluid-fracture boundary remains clearly identifiable from the optical contrast. No fluid-fluid phase separation occurs in any case, and the gray regions between the red and blue contours correspond to fracture formation. Further clarification on phase and region identification based on optical contrast in the images is provided in Sec. I of the Supplemental Material [25]. The fracturing fluids in each image are (a) water, where the fluid front closely follows the fracture front with minimal lag at all time and the fracture front remains smooth; (b) 95 wt % glycerol-water mixture with a viscosity of 0.43 Pa s, where the fluid front lags significantly behind the fracture front at all time and the fracture front exhibits a steplike pattern due to intermittent breaks and large break amplitudes; (c) Polymer 1 with a molecular weight of 20M g/mol and a viscosity of 0.43 Pa s, and the fracture front remains smooth, similar to the behavior observed with water; (d) Polymer 2 with a molecular weight of 4M g/mol and a viscosity of 0.39 Pa s, where the fluid front and the fracture front are very close, and the fracture front remains smooth, also similar to the behavior observed with water; (e) Polymer 3 with a molecular weight of 1M g/mol and a viscosity of 0.63 Pa s, where the fluid front lags slightly behind the fracture front and the fracture front exhibits a steplike pattern with smaller break amplitudes and more frequent break events compared to the 95 wt % glycerol-water mixture; and (f) Polymer 4 with a molecular weight of 200k g/mol and a viscosity of 0.61 Pa s, where the fluid front lags further behind the fracture front but with smaller lag compared to the 95 wt % glycerol-water mixture, and the fracture front exhibits a steplike pattern with smaller amplitudes and more frequent break events compared to the 95 wt % glycerol-water mixture. The fracturing fluids used in panels (b)–(f), including four polymer solutions and a glycerol-water mixture, are selected to have comparable viscosities at the low shear rate at which they were characterized.

molecular weight polymer solution. The fluid front again closely follows the fracture front throughout the fracturing process, exhibiting a behavior similar to that of the higher molecular weight polymer solution, as shown in Fig. 2(d). Both fronts propagate smoothly with a consistently small lag, as seen in the kymograph in Fig. 3(d). Thus, both polymer solutions exhibit behavior similar to that of water, despite their much higher viscosities measured at low shear rates.

To further investigate the behavior of polymer solutions, we conduct additional experiments using two more solutions prepared from different polymers, both with a molecular weight of 20M g/mol. We prepare the two solutions at higher concentrations of 0.5 and 0.25 wt %; their viscosities are 0.6 and 0.4 Pa s at a low shear rate of $1\,s^{-1}$, respectively. In both cases, the fluid front remains close to the fracture front, maintaining a consistently small lag similar to that observed for the lower concentration polymer solution. We plot the lag length for each polymer solution as a function of viscosity measured at low shear rate. Despite their much higher viscosities, all polymer solutions exhibit lag distances comparable to water, which has much lower viscosity, as indicated by the data points along the dashed blue line in Fig. 4(a). These are all substantially smaller than those observed for Newtonian fluids of similar viscosity, represented by the red circles as shown in Fig. 4(a). Thus, despite their much higher viscosities, polymer solutions behave in the same manner as water in hydrofracturing.

III. SHEAR THINNING OF POLYMER SOLUTIONS

To evaluate the flow behavior of polymer solutions, we examine the shear behavior near the advancing fracture tip. We compare the timescale over which a shear-driven velocity profile develops to the timescale over which the fluid catches

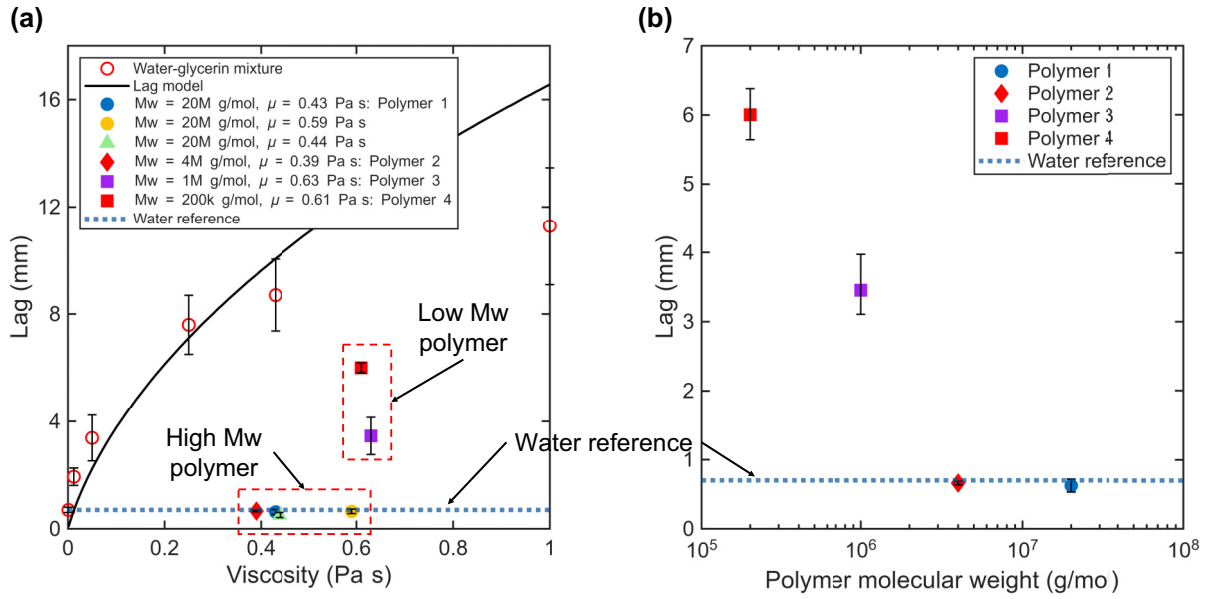

FIG. 4. Lag length between fluid and the fracture fronts against (a) fluid viscosity at low shear and (b) polymer molecular weight. (a) Lag length against viscosity for various fluids, including glycerol-water mixtures with varying glycerol content and solutions of polymers with different molecular weights. The solid black line denotes the lag length predicted by an analytical model developed for Newtonian fluids. The lag length of water is used as the reference, represented by the blue dotted line. Solutions of polymers with high molecular weights of 20M and 4M g/mol, labeled as "High Mw polymer," exhibit a small lag, comparable to that of water. In contrast, solutions of polymers with lower molecular weights of 1M and 200k g/mol, labeled as "Low Mw polymer," exhibit significantly larger lags, though these lags remain smaller than those of glycerol-water mixtures with similar viscosities. The data highlight a clear deviation from the Newtonian fluid model, especially for polymers with high molecular weights. (b) The lag length decreases with increasing polymer molecular weight. Polymers with molecular weights exceeding 4M g/mol, as shown in this plot, exhibit small lags comparable to that of water, as indicated by the blue dotted reference line.

up during a single break event. The latter is estimated as $t_f = \frac{L_{\text{break}}}{u}$, where L_{break} is the average break size of 0.4 μm (see Sec. II of the Supplemental Material [25]) and u is the fluid front velocity of 10 m/s, yielding $t_f = 40$ μs. For the high-molecular-weight polymer solutions, the time for the development of the velocity profile is estimated using the viscous diffusion time across the fracture width $t_v = \frac{\rho_p (0.5h)^2}{\pi^2 \mu_p}$, where h is the local fracture width, μ_p is the dynamic viscosity, and ρ_p is the fluid density. We estimate the local fracture thickness to be 6 μm, assuming a linear increase in fracture width from the tip (see Sec. III of the Supplemental Material [25]). Assuming μ_p to be that of water, 0.001 Pa s, and ρ_p to be 1000 kg/m^3, the viscous diffusion time is 1 μs. Any viscosity increase due to polymers would only further shorten this diffusion time. Since t_f is an order of magnitude longer than t_v, the polymer solution has enough time to develop a full shear-driven velocity profile across the fracture. For a gap of $h = 6$ μm and an average velocity of 10 m/s, the average shear rate is estimated as $\dot{\gamma}_{\text{avg}} = \frac{u}{h} \sim 10^6$ m/s.

To account for the observed flow behavior of the polymer solutions given the calculated shear rates, we measure their shear-dependent viscosity using a rotational rheometer (TA Instrument ARES-G2). A solution of the polymer with a high molecular weight of 20M g/mol exhibits pronounced shear thinning with viscosity following a power-law relation $\mu \propto \dot{\gamma}^{-0.6}$ (see Sec. IV of the Supplemental Material [25]), as shown by the blue circles in Fig. 5. Extrapolating this trend to 10^6 s^{-1} yields a viscosity of 2×10^{-4} Pa s, which is unphysical, as viscosity cannot fall below that of water; instead, the viscosity likely approaches that of water at high shear. This pronounced shear thinning accounts for the behavior observed for the fracture, where the fluid lag is minimal, similar to that of water, as shown in Fig. 2(c). A solution of a polymer with a molecular weight of 4M g/mol exhibits similar shear-thinning behavior following a similar power law (see Sec. IV of the Supplemental Material [25]), as shown by the green diamonds in Fig. 5. Extrapolation of the power-law relation gives a viscosity of 1×10^{-3} Pa s at 10^6 s^{-1}, close to that of water. This again accounts for the fact that the behavior of fracture is similar to that of water.

To further explore the impact of shear thinning on the fracture and flow behavior, we perform additional tests using solutions of polymers with lower molecular weights. We set the low-shear viscosities of these solutions to match those of the solutions of high-molecular-weight polymers; however, the solutions of polymers with lower molecular weights exhibit significantly less shear thinning. The polymer concentrations used in this work are not high enough to form rigid gels; consequently, all polymer solutions remain fluidic in nature. A solution of a polymer with a molecular weight of 1M g/mol exhibits a viscosity of 0.1 Pa s at the highest measured shear rate of 10^3 s^{-1}, indicating moderate shear thinning, as shown by the yellow squares in Fig. 5. In a fracturing experiment, this solution behaves qualitatively differently from water; it shows a consistently larger fluid lag of ∼3 mm, as seen in the fracture image in Fig. 2(e) and the kymograph in

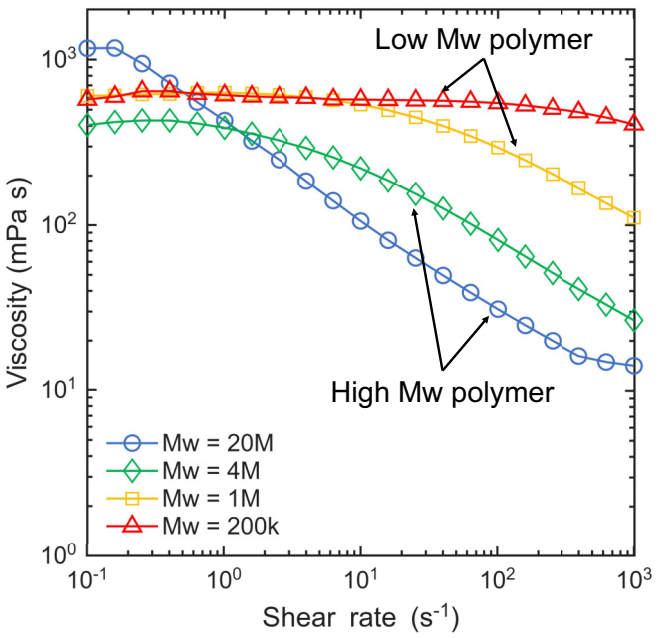

FIG. 5. Viscosity vs shear rate for solutions of polymers with varying molecular weights. Solution of polymers with high molecular weights of 20M and 4M g/mol, labeled as "High Mw polymer," exhibit strong shear-thinning behavior, with viscosity decreasing significantly as shear rate increases. In contrast, solutions of polymer with lower molecular weights of 1M and 200k g/mol, labeled as "Low Mw polymer," exhibit much weaker shear thinning, with only modest reductions in viscosity as the shear rate increases.

Fig. 3(e). Although the lag and break amplitudes are larger than those of the solutions of high-molecularweight polymers, they remain smaller than those of glycerol-water mixtures due to the remnant shear thinning. A solution of a polymer with an even lower molecular weight of 200k g/mol exhibits much weaker shear thinning with the viscosity decreasing to 0.4 Pa s at a shear rate of $10^3\,s^{-1}$, as shown by the red triangles in Fig. 5. It results in a lag of ~ 6 mm and large break amplitudes, as shown in the fracture image in Fig. 2(f) and the kymograph in Fig. 3(f). Both lag and break amplitudes are the largest among the tested polymer solutions.

To estimate the effective viscosity of the polymer solution in hydrofracture, we use the measured lag and compare it to the value expected from the analytical lag-viscosity model for Newtonian fluids developed in Ref. [19], shown as the black line in Fig. 4. For a solution of polymer with a molecular weight of 1M g/mol, the effective viscosity is estimated to be 0.08 Pa s (see Sec. V of the Supplemental Material [25]), higher than the extrapolated value of 0.007 Pa s at a shear rate of $10^6\,s^{-1}$ (see Sec. IV of the Supplemental Material [25]). For a solution of a polymer with a lower molecular weight of 200k g/mol, the estimated effective viscosity is 0.2 Pa s, in closer agreement with the extrapolated viscosity of 0.13 Pa s at a shear rate of $10^6\,s^{-1}$.

These results suggest that the shear-thinning behavior that occurs at the high shear rates of the fluid flow during hydrofracturing leads to the observed flow and fracture behavior. As polymer molecular weight increases, shear thinning becomes more pronounced, leading to smaller fluid lag, as shown by the monotonic decrease in lag length with molecular weight in Fig. 4(b). For solutions of polymer with the highest molecular weight, the shear thinning is so pronounced that the behavior of the fracture is close to that of water. These results underscore the importance of shear thinning in the behavior of hydrofracture.

IV. CONCLUSIONS

We investigate the effects of polymer solutions on the coupled flow and fracture dynamics near the tip of a propagating hydrofracture using high-speed imaging. The results show that solutions of polymers with high molecular weights, and high viscosity at low shear rate, exhibit minimal fluid lag and small break amplitudes, similar to the behavior of low-viscosity Newtonian fluids. In contrast, viscous Newtonian fluids, such as glycerol-water mixtures, with viscosities similar to those of the solutions of high-molecular-weight polymers, exhibit significant fluid lag and larger break amplitudes during fracture propagation. This contrast arises from strong shear thinning in the polymer solutions, which markedly reduces their effective viscosity under the high-shear conditions of the hydrofracture near the tip. For solutions of polymers with lower molecular weights where shear thinning is weaker, the fluid lag and fracture behavior approach those of conventional viscous Newtonian fluids. The shear thinning of polymer solutions near the fracture tip modifies local flow conditions compared to regions farther away, where viscosity remains higher due to lower shear rates; this behavior affects proppant transport and distribution within the fracture, particularly in the advancing regions near the tip. These findings highlight the critical role of fluid rheology in governing flow and fracture dynamics and offer insights for optimizing fracturing fluids in hydraulic fracturing applications.

ACKNOWLEDGMENTS

We thank all our collaborators for their contributions to this work. In particular, we are grateful to Dr. Howard Stone for the valuable discussions on flow dynamics within a fracture.

DATA AVAILABILITY

The data that support the findings of this article are openly available [31]; embargo periods may apply.

[1] E. Detournay, Mechanics of hydraulic fractures, Annu. Rev. Fluid Mech. **48**, 311 (2016).

[2] P. D. Bons, M. A. Elburg, and E. Gomez-Rivas, A review of the formation of tectonic veins and their microstructures, J. Struct. Geol. **43**, 33 (2012).

[3] T. Sharmin, N. R. Khan, M. S. Akram, and M. M. Ehsan, A state-of-the-art review on geothermal energy extraction, utilization, and improvement strategies: Conventional, hybridized, and enhanced geothermal systems, Int. J. Thermofluids **18**, 100323 (2021).

[4] Y. Jia, C.-F. Tsang, A. Hammar, and A. Niemi, Hydraulic stimulation strategies in enhanced geothermal systems (EGS): A review, Geomech. Geophys. Geo-energ. Geo-resour. **8**, 211 (2022).

[5] H. Belyadi, E. Fathi, and F. Belyadi, *Hydraulic Fracturing in Unconventional Reservoirs: Theories, Operations, and Economic Analysis*, 2nd ed. (Gulf Professional Publishing, Houston, USA, 2019).

[6] C. T. Montgomery and M. B. Smith, Hydraulic fracturing: History of an enduring technology, J. Pet. Technol. **62**, 26 (2010).

[7] R. Barati and J.-T. Liang, A review of fracturing fluid systems used for hydraulic fracturing of oil and gas wells, J. Appl. Polym. Sci. **131**, 40735 (2014).

[8] Q. Li, H. Xing, J. Liu, and X. Liu, A review on hydraulic fracturing of unconventional reservoir, Petroleum **1**, 8 (2015).

[9] S. L. Brantley and A. Meyendorff, *The Facts on Fracking* (New York Times, New York City, NY, USA, 2013).

[10] S. Zhang, F. Wei, P. Liu, L. Shao, and W. Li, Plugging mechanisms of polymer gel used for hydraulic fracture water shutoff, e-Polymers **20**, 411 (2020).

[11] B. Chandra, V. Shankar, and D. Das, Early transition, relaminarization and drag reduction in the flow of polymer solutions through microtubes, J. Fluid Mech. **885**, A47 (2020).

[12] S. Al-Hajri, B. M. Negash, M. M. Rahman, M. Haroun, and T. M. Al-Shami, Perspective review of polymers as additives in water-based fracturing fluids, ACS Omega **7**, 7431 (2022).

[13] J. Schurz, Rheology of polymer solutions of the network type, Prog. Polym. Sci. **16**, 1 (1991).

[14] G. Marrucci, F. Greco, and G. Ianniruberto, Rheology of polymer melts and concentrated solutions, Curr. Opin. Colloid Interface Sci. **4**, 283 (1999).

[15] R. G. Larson, The rheology of dilute solutions of flexible polymers: Progress and problems, J. Rheol. **49**, 1 (2005).

[16] G. B. Thurston, Shear rate dependence of the viscoelasticity of polymer solutions: I. Theoretical model, J. Non-Newton. Fluid Mech. **9**, 57 (1981).

[17] P. E. Rouse Jr. and K. Sittel, Viscoelastic properties of dilute polymer solutions, J. Appl. Phys. **24**, 690 (1953).

[18] J. D. Ferry, Viscoelastic properties of polymer solutions, J. Res. Natl. Bur. Stand. **41**, 53 (1948).

[19] T. Cochard, I. Svetlizky, G. Albertini, R. C. Viesca, S. M. Rubinstein, F. Spaepen, C. Yuan, M. Denolle, Y.-Q. Song, L. Xiao, and D. A. Weitz, Propagation of extended fractures by local nucleation and rapid transverse expansion of crack-front distortion, Nat. Phys. **20**, 660 (2024).

[20] X. Wei, C. Li, C. McCarthy, and J. M. Kolinski, Complexity of crack front geometry enhances toughness of brittle solids, Nat. Phys. **20**, 1009 (2024).

[21] C.-Y. Lai, B. Rallabandi, A. Perazzo, Z. Zheng, S. E. Smiddy, and H. A. Stone, Foam-driven fracture, Proc. Natl. Acad. Sci. USA **115**, 8082 (2018).

[22] P. Liu, Y. Ju, P. G. Ranjith, Z. Zheng, L. Wang, and A. Wanniarachchi, Visual representation and characterization of three-dimensional hydrofracturing cracks within heterogeneous rock through 3D printing and transparent models, Int. J. Coal Sci. Technol. **3**, 284 (2016).

[23] A. A. Savitski and E. Detournay, Propagation of a penny-shaped fluid-driven fracture in an impermeable rock: Asymptotic solutions, Int. J. Solids Struct. **39**, 6311 (2002).

[24] I. Svetlizky, D. S. Kammer, E. Bayart, G. Cohen, and J. Fineberg, Brittle fracture theory predicts the equation of motion of frictional rupture fronts, Phys. Rev. Lett. **118**, 125501 (2017).

[25] See Supplemental Material at http://link.aps.org/supplemental/10.1103/p4bp-b8bz for details of optical contrast-based phase and region identification from the images (Sec. I), break size measurement (Sec. II), fracture thickness estimation (Sec. III), shear rate-viscosity correlations (Sec. IV), and effective viscosity extrapolation (Sec. V).

[26] C. Binetti, G. Florio, N. M. Pugno, S. Giordano, and G. Puglisi, Thermal fluctuations effects on crack nucleation and propagation, J. Mech. Phys. Solids **201**, 106157 (2025).

[27] A. Cannizzo and S. Giordano, Thermal effects on fracture and the brittle-to-ductile transition, Phys. Rev. E **107**, 035001 (2023).

[28] M. R. Buche and S. J. Grutzik, Statistical mechanical model for crack growth, Phys. Rev. E **109**, 015001 (2024).

[29] D. Peck, M. Wrobel, M. Perkowska, and G. Mishuris, Fluid velocity based simulation of hydraulic fracture: A penny shaped model—Part I: The numerical algorithm, Meccanica **53**, 3615 (2018).

[30] D. Peck, M. Wrobel, M. Perkowska, and G. Mishuris, Fluid velocity based simulation of hydraulic fracture—A penny shaped model. Part II: New, accurate semi-analytical benchmarks for an impermeable solid, Meccanica **53**, 3637 (2018).

[31] Y. Du, T. Cochard, I. Svetlizky, C. Yuan, Y.-Q. Song, L. Xiao, and D. A. Weitz, Data for "Effects of polymer solutions on hydraulic fracture", Zenodo, 2026, https://doi.org/10.5281/zenodo.18193035.

Correction: A typographical error in the value given for pressure in the second paragraph of Sec. II has been fixed.